RSC Advances

PAPER

View Article Online
View Journal | View Issue

Cite this: *RSC Adv.*, 2022, **12**, 30145

Fe/N codoped porous graphitic carbon derived from macadamia shells as an efficient cathode oxygen reduction catalyst in microbial fuel cells†

Haoming Ning,[ab] Zhi Zhang, *[ab] Chunhai Shi,*[c] Xiaolei Ma,[c] Jian Li,[c] Hongyi Zhu[ab] and Jiawei Hu[ab]

In this study, Fe/N codoped porous graphitic carbon derived from macadamia shells was prepared at different temperatures as cathodic catalysts for microbial fuel cells (MFCs), with K_2FeO_4 as a bifunctional catalyst for porosity and graphitization. The catalyst prepared at 750 °C (referred to as MSAC-750) showed a large specific surface area (1670.3 $m^2\ g^{-1}$), graphite structure, and high pyridine-N and Fe-N_X contents. Through the electrochemical workstation test, MSAC-750 shows excellent oxygen reduction reaction (ORR) activity, with an onset potential of 0.172 V and a half-wave potential of −0.028 V (*vs.* Ag/AgCl) in a neutral medium, and the ORR electron transfer number is 3.89. When applied to the MFCs as cathodic catalysts, a higher maximum power density and voltage of 378.68 mW m^{-2} and 0.425 V were achieved with the MSAC-750 catalyst and is superior to that of the Pt/C catalyst (300.85 mW m^{-2} and 0.402 V). In this case, a promising method is hereby established for the preparation of an excellent electrochemical catalyst for microbial fuel cells using inexpensive and easily available macadamia shells.

Received 8th July 2022
Accepted 13th October 2022

DOI: 10.1039/d2ra04214b

rsc.li/rsc-advances

1. Introduction

Microbial fuel cells (MFCs) are a clean and sustainable energy technology capable of degrading organic matter in wastewater and generating electricity.[1] Compared with the typical two-chamber MFC, the single-chamber MFC with an air cathode has attracted the attention of a large number of researchers because of its low cost, simple structure, and good power generation effect.[2] However, the power output performance of a single-chamber MFC is not ideal due to the high overpotential and sluggish kinetic rate of the oxygen reduction reaction (ORR) on its air cathode. Although the commercial Pt/C catalyst is provided with good ORR activity, its high cost and poor stability severely limit its large-scale application in MFCs.[3,4] Therefore, finding a low-cost, efficient and stable MFC cathode oxygen reduction catalyst is a goal worthy of attention.

In recent years, biomass has been increasingly used as a precursor of carbon materials by researchers because of its low cost and easy availability. According to these studies, biomass carbon prepared from biomass materials (such as corn straw,[5] waste lotus seed pod,[6] watermelon peel,[7] and eggplant[8]) through certain chemical reactions can be used as a catalyst for oxygen reduction reactions, and is endowed with great catalytic potential. For biomass carbon materials, rich porosity and high specific surface area (SSA) can increase the contact area between the electrolyte and electrode, expose more ORR active sites in carbon materials, and enhance the catalytic kinetics of the ORR.[9,10] KOH, K_2CO_3, and other chemical reagents are generally adopted to activate carbon materials to obtain layered porous structures with a high specific surface area. For example, Sun *et al.* activated mushroom biomass using K_2CO_3 to obtain activated carbon with a specific surface area of 2330 $m^2\ g^{-1}$, which is provided with a good pollutant adsorption capacity.[11] Zhu *et al.* activated tea residue with KOH to obtain carbon materials with a hierarchical porous structure and good ORR capability.[10] At the same time, the high conductivity of carbon materials is also necessarily important for ORR activity. Improving the graphitization degree of carbon materials can achieve a high conductivity that promotes charge transfer.[12] According to relevant studies, the graphitization of biomass carbon materials can be fulfilled at a lower temperature (<1000 °C) by using Fe, Co, Mn, or Ni species as catalysts.[13]

In addition to adjusting the porosity and improving the graphitization structure, the implantation of heteroatoms (such as N and Fe atoms) into carbon materials is another effective strategy to improve catalytic performance, which can provide more ORR active sites for carbon materials.[14] Among them, pyridine-N can reduce the binding energy of O–O bonding and promote the ORR process, graphite-N can promote electron

[a]*Key Laboratory of Three Gorges Reservoir Region's Eco-Environment, Ministry of Education, Chongqing University, Chongqing, 400045, China. E-mail: zhangzhicqu@cqu.edu.cn*

[b]*College of Environment and Ecology, Chongqing University, Chongqing, 400045, China*

[c]*Northwest China Municipal Engineering Northwest Design and Research Institute, Lanzhou 730000, China. E-mail: 252440589@qq.com*

† Electronic supplementary information (ESI) available. See DOI: https://doi.org/10.1039/d2ra04214b

transport and improve the conductivity of carbon materials, and Fe-N_X can promote the adsorption of oxygen and the fracture of the O–O bonding.[15,16] Wang *et al.* prepared nitrogen-doped biomass carbon material (NC-800) with green foxtail grass taken as a biomass precursor by adding melamine for pyrolysis. MFCs using this catalyst have a higher power density than commercial Pt/C.[9] Gao *et al.* synthesized Fe, N codoped mesoporous carbon (FeNMC) as a cathode catalyst at 900 °C with biomass flour, dicyanamide, and anhydrous ferric chloride as the carbon source, nitrogen source, and iron source, respectively. Among them, FeNMC-2 presents a positive half-wave potential of 0.885 V.[17] These studies show that heteroatom doping can improve the ORR catalytic effect of carbon materials.

In this study, Fe/N codoped porous graphitic carbon derived from macadamia shell (MSAC) under different activation temperatures was developed by adding K_2FeO_4 and urea as activators. K_2FeO_4 is decomposed into KOH and Fe species at high temperatures, which are used as activators and graphitization catalysts for biomass carbon materials, respectively.[13] At the same time, the application of K_2FeO_4 and urea as the Fe source and N source adds more ORR active sites to the carbon materials. The whole synthesis process is simple, inexpensive, and green. The prepared MSAC-750 not only has a hierarchical porous structure with a high specific surface area but also contains a certain amount of Fe-N_X and graphite structure. Thanks to these favorable characteristics, MSAC-750 shows excellent ORR electrocatalytic activity and provides considerable power output in a single-chamber MFC with an air cathode.

2. Materials and methods

2.1 Materials

Potassium ferrate (K_2FeO_4), urea ($CO(NH_2)_2$), anhydrous sodium acetate, ethanol and hydrochloric acid (HCl) were purchased from Chengdu Kelong Chemical Reagent Factory; W1S1005 carbon cloth, 0.5 wt% Nafion (D-520, DuPont), and 20 wt% Pt/C were bought from Shanghai Hesen Electric Co., Ltd; Polytetrafluoroethylene (PTFE, solid content: 60%) was purchased from Shanghai Aladdin Chemical Reagent Factory; The high purity gases of O_2 (99.99%) and N_2 (99.99%) were obtained from Chongqing Chaoyang Gas Co., Ltd. (Note: All these chemical reagents were used directly without further purification).

2.2 Synthesis of MSAC catalysts

Macadamia nuts were bought from the local market. The waste macadamia shells were washed with deionized water, and were then dried. Afterwards, the macadamia shell was put into a tubular furnace and carbonized at 300 °C under nitrogen protection. The carbonized macadamia shell biomass carbon was ground and screened on a 200 mesh screen. Referring to the previous literature,[13] 5 g of screened carbon powder was immersed in 500 mL of 10 g L^{-1} urea solution, stirred continuously for 8 hours until fully mixed, and dried in an oven at 60 °C. Then, the dried product was immersed in 10 g/200 mL of K_2FeO_4 solution and stirred magnetically for 8 hours. Next, the dried solid mixture was put into a tubular furnace and heated to the set temperature under N_2 protection, and the heating rate was 5 °C min^{-1}. It was further heated for 120 min at the set temperature (including 600, 700, 800, and 900 °C), and the situation at an additional temperature of 750 °C was studied according to the subsequent experimental results. After natural cooling to room temperature, the product was washed with 1 M HCl solution to remove excess impurities. The product was prepared after being repeatedly washed to neutral with deionized water and dried at 70 °C for 8 hours.

The obtained carbon material is denoted as MSAC-T, where T is the activation temperature (T = 600, 700, 750, 800, 900). In addition, under the same synthetic conditions as MSAC-750, two groups of control samples with only urea or only K_2FeO_4 were prepared and named MSAC-N and MSAC-Fe, respectively.

2.3 Material characterization

The microstructure and surface morphology of the prepared materials were characterized by scanning electron microscopy (SEM, ZEISS Gemini 300, Germany) with an attached energy dispersive X-ray spectrometry (EDS) system and TEM (TF20). The nitrogen adsorption/desorption test was performed at liquid nitrogen temperature (77 K) on a physical adsorption apparatus (ASAP2460, Micromeritics Instruments, USA) to obtain the pore size distribution and specific surface area. Moreover, X-ray diffraction (XRD, Rigaku Smartlab, Japan) was performed in the 2θ range of 10–90° with Cu Kα radiation, while Raman spectroscopy (Horiba LabRAM HR Evolution, Japan) was conducted at an excitation wavelength of 532 nm. To analyze the chemical composition of the material, X-ray photoelectron spectroscopy (XPS, Thermo Scientific K-Alpha, USA) was performed on an X-ray diffractometer equipped with a monochromatic Al Kα source ($h\nu$ = 1486.6 eV).

2.4 Electrochemical characterization

The cyclic voltammetry (CV) and Tafel curves of the prepared carbon materials were obtained using a CHI 660E potentiostat (CH Instruments, Chenhua, Shanghai, China), with three-electrode test equipment used for electrochemical testing. A method from previous literature was adopted for preparing the catalyst ink.[10] The ink was dropped on the glassy carbon electrode and dried at room temperature to participate in the test. Among them, the CV test was conducted at a scanning rate of 5 mV s^{-1} within the potential range of 0.4 V to −0.8 V. The Tafel curve was obtained by scanning the overpotential range of 0–120 mV at a scanning rate of 1 mV s^{-1}, and the exchange current density (i_0) was calculated according to the Tafel curve in the overpotential range from 80 to 120 mV. The catalytic stability of ORR was characterized by chronoamperometry (CA) in O_2 saturated 50 mM PBS solution at a constant potential of −0.30 V for 10 000 s, and the speed of the rotating disk electrode (RDE) was 1600 rpm.

Additionally, the prepared catalyst was tested by a rotating ring disk electrode (RRDE). For the RRDE test, a ring disk electrode (E7R9, PINE, USA) was used as the working electrode,

an Ag/AgCl electrode was used as the reference electrode, and a platinum plate electrode was used as the counter electrode. A linear sweep curve (LSV) was performed in 50 mM phosphate-buffered saline (PBS) solution saturated with O_2 at 1600 rpm. The H_2O_2 yield and ORR electron transfer number (n) were calculated according to the following formula:[18]

$$n = \frac{4I_d}{I_r/N + I_d} \quad (1)$$

$$H_2O_2\% = \frac{200I_r/N}{I_r/N + I_d} \times 100\% \quad (2)$$

where N is the ring collection efficiency of the Pt ring ($N = 0.37$), and I_d and I_r are the disk and ring currents, respectively.

2.5 Construction and operation of microbial fuel cells

A single-chamber MFC with an inner volume of 28 mL was assembled with plexiglass. The details of the fabrication of the air cathodes are listed in the Text S1.† The MFC anode was made of carbon felt and connected to the cathode through an external resistance of 1000 Ω and a titanium wire. Then, the cultivation of MFC began after the assembly of MFC was complete. The anode was inoculated using anaerobic sludge collected from a wastewater treatment plant (Chongqing, China). Anhydrous sodium acetate (1 g L^{-1}), vitamin solution (5 ml L^{-1}), and trace mineral solution (12.5 ml L^{-1}) were added to 50 mM PBS to obtain MFC nutrient solution. The contents of PBS, vitamin solution, and trace mineral solution in the experiment are listed in Table S1.† All the MFCs were run in the fed-batch process by replacing the nutrient solution when the voltage was lower than 50 mV.

The cell voltage was recorded every 1 min at the external resistance by a data acquisition system (DAS, PISO-813. Hongge Co. Ltd., Taiwan). The polarization curves and power density of MFCs were acquired by adjusting the external resistance from 9000 to 10 Ω, and the power density was normalized to the cathode surface area. The MFCs were placed under open circuit potential for at least 6 h before testing. Besides, the anode and cathode voltages were obtained by using a saturated calomel electrode (SCE) as the reference electrode. The calculation formulas of the COD removal rate and coulombic efficiency (CE) of pollutants by MFC were the same as those described in the literature.[9] All tests were conducted in duplicate, and the mean values are presented.

3. Results and discussion

3.1 Material characterization

The formation of the pore structure of the material mainly utilizes the following mechanisms, as shown in eqn (3)–(8). First, K_2FeO_4 starts to react and be decomposed at 300 °C to form $Fe(OH)_3$, KOH, Fe_2O_3, and K_2O.[19] KOH, known as the most common activator of carbon materials, can be reduced by C in biomass carbon materials to form pores in the materials. When the temperature continues to rise, KOH and K_2CO_3 will begin to be decomposed into K_2O, H_2O, and CO_2. K_2O can also be reduced to K and CO by C in the material at high temperatures. In conclusion, both KOH and K_2O can react with C in the material to etch the carbon atomic layer and to finally form a rich pore structure in the biomass carbon material.[20,21]

$$4K_2FeO_4 + 10H_2O \rightarrow 4Fe(OH)_3 + 8KOH + 3O_2 \quad (3)$$

$$4K_2FeO_4 \rightarrow 2Fe_2O_3 + 4K_2O + 3O_2 \quad (4)$$

$$C + 4KOH \rightarrow K_2O + K_2CO_3 + 2H_2 \quad (5)$$

$$2KOH \rightarrow K_2O + H_2O \quad (6)$$

$$K_2CO_3 \rightarrow K_2O + CO_2 \quad (7)$$

$$C + K_2O \rightarrow 2K + CO \quad (8)$$

Fig. 1(a)–(f) shows the surface morphology of the MSAC catalyst at different activation temperatures. Among them, micropores can be observed on the surface of MSAC-600, indicating that the activator has begun to play a role in pore formation on carbon materials. With the increase in the activation temperature, the pores on the surface of carbon materials become larger and rougher, and an increasingly dense porous structure appears until the appearance of the MSAC-750 surface. This is helpful for MSAC-750 to provide a channel and place for ORR when it is used as a cathode oxygen reduction catalyst of MFC.[22] However, as the activation temperature continues to rise, the surface of MSAC-800 and MSAC-900 mainly presents mesoporous and even macro-porous structures, which indicates the collapsing tendency of the pore structure. The SEM images of MSAC-N and MSAC-Fe are shown in Fig. S1(a and b).† A few holes are observed on the surface of the MSAC-N material, while the MSAC-Fe pore structure is basically formed, suggesting the major role of K_2FeO_4 as the activator in the formation of material pores. Additionally, the EDS image [Fig. 1(g)–(i)] shows that N and Fe elements are successfully doped into the carbon skeleton of MSAC-750. N and Fe elements are very evenly dispersed in the whole sample, and the signals of these two elements overlap each other, which means that the structure of the Fe-N_X configuration may be formed in the MSAC-750 material. By virtue of the transmission electron microscopy (TEM), the microstructure of MSAC-750 can be further visualized. Fig. 1(j) depicts the alternating light and dark stripes, which are caused by the pore structure in the MSAC-750 catalyst. The appearance of lattice stripes with a distance of 0.34 nm is observed in the high-resolution transmission electron microscope (HRTEM) images [Fig. 1(k)], corresponding to the Fe_3C (002) plane.[16]

The pore distribution and specific surface area of the MSAC catalyst were analyzed and studied through the N_2 adsorption–desorption test. As shown in Fig. 2(a), only the N_2 adsorption–desorption curve of the MSAC-N catalyst is not affected by the relative pressure, and the adsorption amount is rather limited. This indicates that only a few pores are formed on the carbon material without K_2FeO_4 activation, and that most of its structure is not activated. Therefore, its specific surface area is rather small, which is consistent with the SEM image. In addition, other MSAC-T and MSAC-Fe catalysts present combined

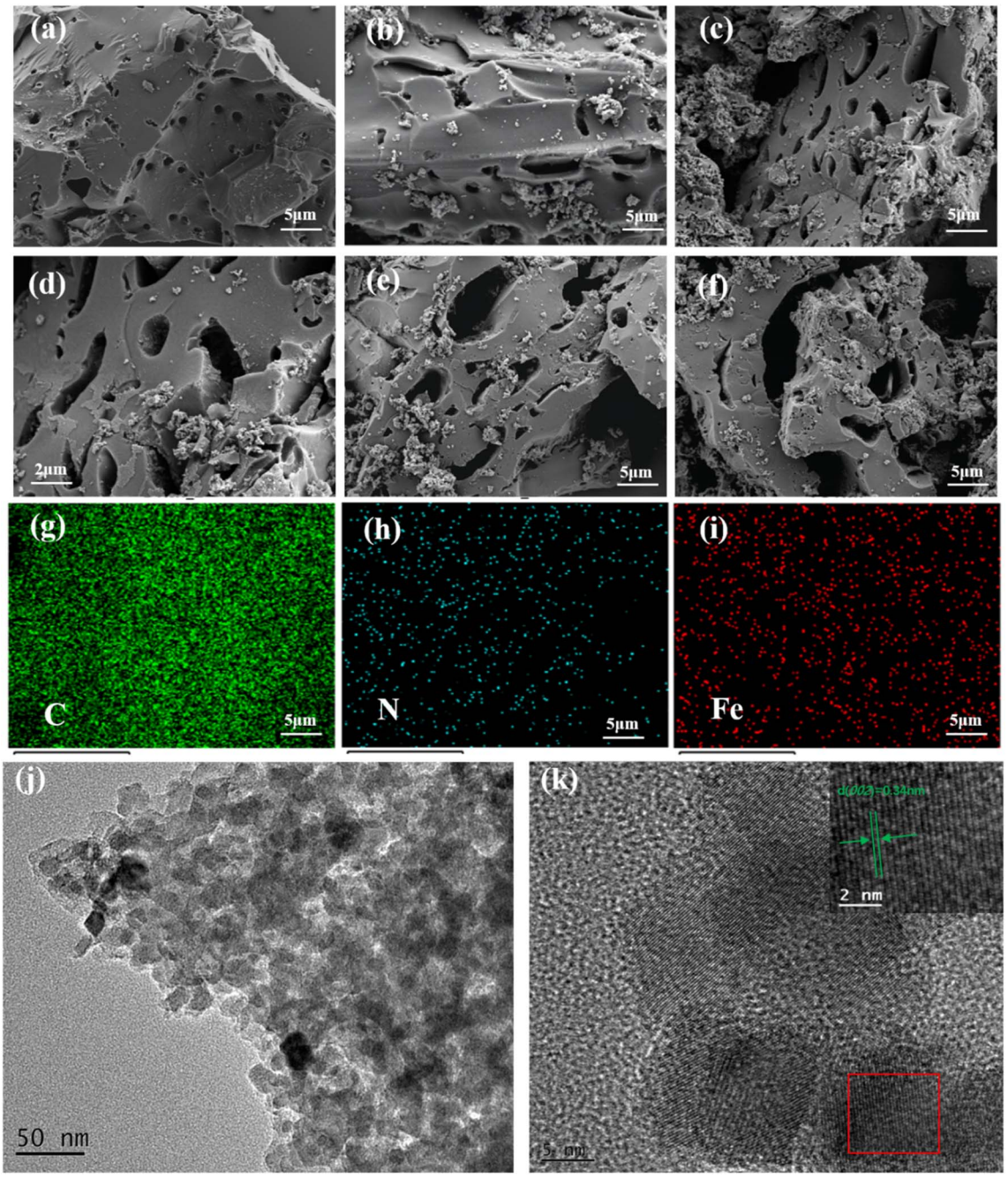

Fig. 1 SEM images of (a) MSAC-600, (b) MSAC-700, (c and d) MSAC-750, (e) MSAC-800, and (f) MSAC-900; element mapping images of (g) C, (h) N, (i) Fe, and (j and k) TEM images of MSAC-750.

isotherms of type I and type IV, indicating that micropores and mesopores coexist in the carbon materials activated by K_2FeO_4. Among them, MSAC-750 has a relatively obvious H_4-type mesoporous hysteresis loop, indicating that its internal micropores and mesopores are evenly distributed.[23] Table 1 summarizes the specific surface area and pore distribution of MSAC materials at different activation temperatures. With the gradual increase in the temperature, the specific surface area (1670.3 $m^2\ g^{-1}$) of MSAC-750 increases by nearly 120% compared with that of MSAC-600 (760.4 $m^2\ g^{-1}$). When the temperature rises to 900 °C, the specific surface area of MSAC-900 decreases to 1223.9 $m^2\ g^{-1}$. This is because before the temperature reaches 750 °C, KOH generated by K_2FeO_4 reacts continuously with C in the carbon material at high temperatures, creating many cavities in the carbon material. However, when the temperature rises from 750 °C to 900 °C, these previously created micropores collapse and are transformed into mesoporous or even macro-porous structures, thus resulting in a decline in the overall specific surface area of carbon materials.[24] As shown in Fig. 2(b), the pore-forming direction of KOH generated by K_2FeO_4 changes

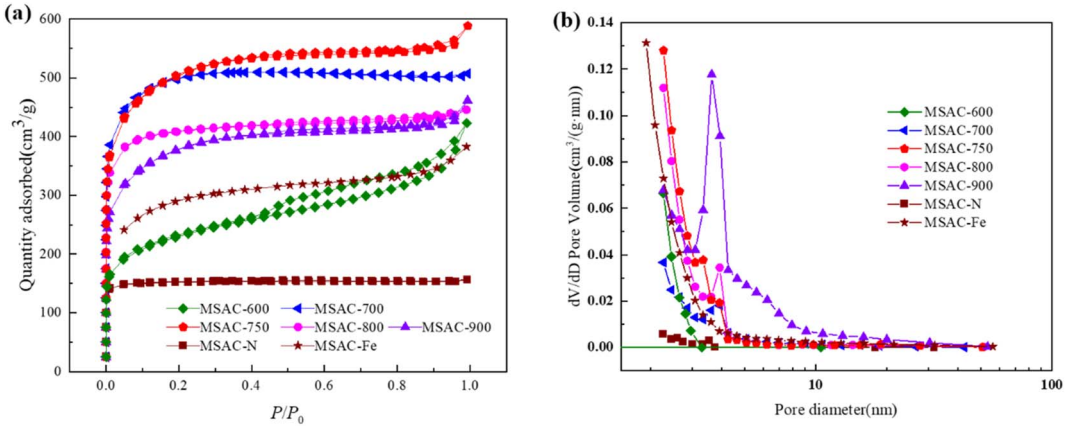

Fig. 2 (a) N_2 adsorption–desorption isotherms, and (b) the pore size distribution curves of the MSAC materials.

Table 1 Pore structural parameters of the samples

Materials	S_{BET}[a] ($m^2\ g^{-1}$)	V_{total}[b] ($cm^3\ g^{-1}$)	V_{micro}[c] ($cm^3\ g^{-1}$)	% V_{micro}	% (V_{meso} + V_{marco})
MSAC-N	449.8	0.243	0.231	95.1	4.90
MSAC-Fe	972.8	0.691	0.581	84.0	16.0
MSAC-600	760.4	0.689	0.523	75.9	24.1
MSAC-700	1524.7	0.784	0.666	84.8	15.2
MSAC-750	1670.3	0.836	0.681	81.4	18.6
MSAC-800	1349.6	0.854	0.589	69.0	31.0
MSAC-900	1223.9	0.910	0.392	43.1	66.9

[a] Specific surface area. [b] Total pore volume. [c] Volume of the micropores.

from micropores to mesopores at high temperatures between 700 °C and 900 °C.

The crystal structure and graphitization degree of the material were studied by XRD. As shown in Fig. 3(a), diffraction peaks can be observed at 26.3° and 44.3° for materials other than MSAC-N, corresponding to the (002) and (101) crystal planes of graphite carbon (JCPDS No. 41-1487), respectively, indicating that the activation of K_2FeO_4 can generate a graphite structure in biochar.[25] In addition, the increase in activation temperature is conducive to the formation of carbon with more graphite structures, which can be confirmed by the fact that the MSAC-900 catalyst material is provided with the sharpest (002) crystal plane diffraction peak. MSAC-750, MSAC-800, and MSAC-900 show diffraction peaks at 26.4° (002), 35.8° (020), and 56.4° (220), which correspond to the diffraction peaks of Fe_3C (JCPDS No. 03-0411).[26] Based on these results, the formation process of Fe_3C can be reasonably inferred as follows: CO, $Fe(OH)_3$, and Fe_2O_3 can be obtained by the decomposition of

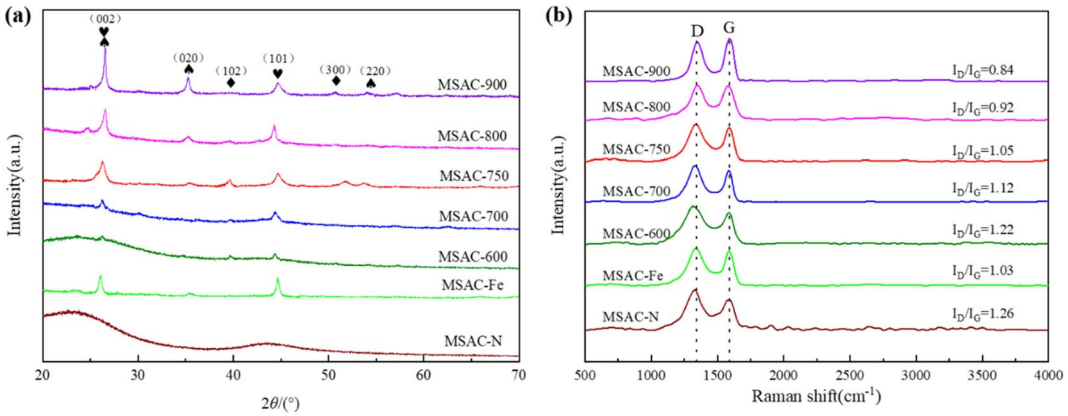

Fig. 3 (a) XRD patterns and (b) Raman spectra of MSAC materials.

K_2FeO_4 at high temperatures. As shown in Eqn. (9)–(11), in the activation process, $Fe(OH)_3$ is first decomposed by heating to form Fe_2O_3, and then the formed Fe_2O_3 is reduced to Fe by CO. With the increasing temperature, Fe and C in the biomass carbon gradually begin to react to form Fe_3C. In this way, iron exists in the biomass carbon structure in the form of Fe_3C. Besides, the diffraction peaks at 40.0° (102) and 49.1° (300) correspond to the peaks of C_3N_4 (JCPDS No. 53-0671).[16] The above data suggest that after the doping and activation of K_2FeO_4 and urea, the amorphous carbon in biomass gradually develops toward graphitization at high temperature and forms Fe–C and N–C compounds inside. These Fe–C and N–C compounds can also be verified in the EDS diagram because it can be seen in the EDS diagram that the signal overlap of C, N, and Fe is high.

$$2Fe(OH)_3 \rightarrow Fe_2O_3 + 3H_2O \quad (9)$$

$$Fe_2O_3 + CO \rightarrow 2Fe + 3CO_2 \quad (10)$$

$$3Fe + C \rightarrow Fe_3C \quad (11)$$

Raman spectroscopy further explains the degree of graphitization. As shown in Fig. 3(b), there are two significant peaks at approximately 1340 cm^{-1} (D-band) and 1580 cm^{-1} (G-band). The D-band is usually characterized by atomic disorder, while the G-band represents the graphite phase. The strength ratio of the D-band to the G-band (I_D/I_G) reflects the graphitization degree, with a smaller I_D/I_G value indicating a higher graphitization degree of carbon materials.[27] The I_D/I_G values of MSAC-600, MSAC-700, MSAC-750, MSAC-800, and MSAC-900 are 1.22, 1.12, 1.05, 0.92, and 0.84, respectively, indicating that the increase in the activation temperature can promote the formation of graphite structures in MSAC materials. The I_D/I_G values of MSAC-N and MSAC-Fe are 1.26 and 1.03, respectively, which also confirms that the Fe species in K_2FeO_4 can make the graphitization structure in carbon materials more orderly at high temperature, while the N species in urea have little effect on the formation of the graphite structure.[28]

Finally, the element composition and bonding state information of each MSAC catalyst was determined by X-ray photoelectron spectroscopy (XPS). As shown in Fig. 4(a), there are C, O, N, and Fe elements in the MSAC-T catalyst, indicating the incorporation of the N and Fe elements into carbon materials, which is consistent with the previous EDS and XRD analysis. Moreover, with the increase in the activation temperature, the content of C increases significantly, while that of N and O decreases gradually. This is because some N- and O-species volatilize from the carbon phase at high temperatures, thus causing more defects.[29]

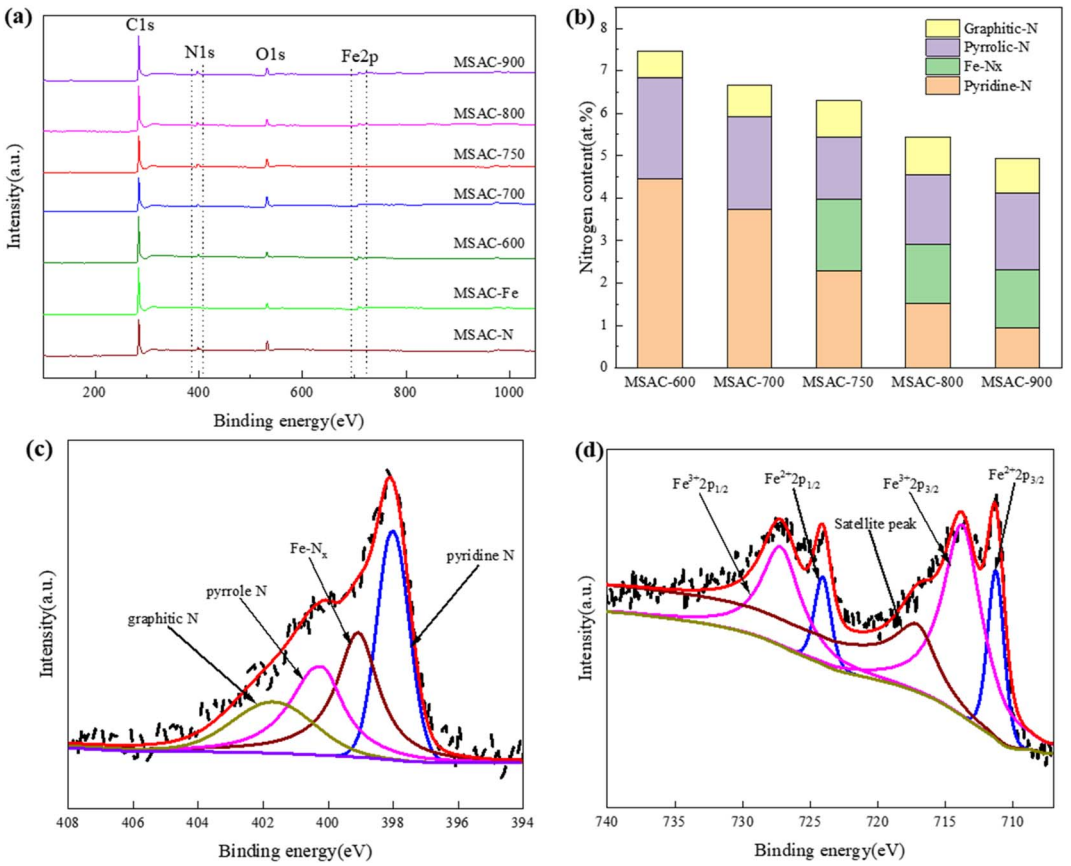

Fig. 4 (a) XPS spectra, (b) nitrogen species contents of MSAC material, (c) high resolution N 1s peaks, and (d) high resolution Fe 2p peaks of MSAC-750.

As shown in Fig. 4(b and c), the N1 s spectrum can be deconvoluted into four characteristic peaks near 398.0, 399.1, 400.3, and 401.6 eV, corresponding to pyridinic-N, Fe-N_X, pyrrolic-N, and graphite-N, respectively.[30] In combination with Fig. 4(b and c) and S2(a–e),† Fe-N_X peaks can only be observed in the N 1s spectra of MSAC-750, MSAC-800, and MSAC-900, which indicates that the Fe element doped in biomass begins to combine with the N element to form Fe-N_X when the temperature is above 700 °C. Fig. 4(b) shows that as the pyrolysis temperature gradually increases, the content of pyridine-N decreases, while the content of graphite-N increases, indicating the change of the nitrogen configuration in the material with the temperature. MSAC-750 presents the lowest pyrrolic-N content (23.21%) and the highest concentrations of pyridinic-N and Fe-N_X (64.32%). Notably, pyridine-N, Fe-N_X, and graphite-N are considered the key active sites of the ORR. Among them, pyridine-N can reduce the binding energy of the O–O bond to promote the ORR process, Fe-N_X is considered to promote the adsorption of oxygen, and the fracture of the O–O bond and graphite-N can enhance the electrocatalytic performance of the material and increase the conductivity in the high energy band. Pyrrole-N is a site that is not conducive to electricity generation, which can reduce O_2 through the $2e^-$ path and generate H_2O_2 that is harmful to the catalyst.[31,32] In this case, three active N species (pyridine-N, graphite-N, and Fe-N_X) have a high content in MSAC-750, which leads to its excellent catalytic activity. As shown in Fig. 4(d) and S3(a–e),† the MSAC catalyst contains four Fe species of Fe^{2+} $2p_{3/2}$ (710.9 eV), Fe^{3+} $2p_{3/2}$ (714.1 eV), Fe^{2+} $2p_{1/2}$ (724.4 eV) and Fe^{3+} $2p_{1/2}$ (727.6 eV) in the Fe 2p spectrum, while there are satellite peaks of MSAC-750, MSAC-800, MSAC-900 and MSAC-Fe near 718.5 eV.[33] Among them, the peak at approximately 710.9 eV is attributed to N-coordinated Fe species, while that at approximately 725.1 eV is caused by the coordination of Fe and C in the material.[30,34] This further confirms that the addition of K_2FeO_4 and urea can realize the codoping of Fe and N in biomass carbon materials.

3.2 Electrochemical activity

The cyclic voltammetry test was carried out in 50 mM PBS solution saturated with N_2 and O_2, and the scanning rate was 5 mV s^{-1}. As shown in Fig. 5(a–f), all MSAC catalysts have no oxygen reduction peak in N_2-saturated PBS solution, while all Pt/C, MSAC-700, MSAC-750, MSAC-800, and MSAC-900 show an obvious oxygen reduction peak in the O_2-saturated PBS solution, proving their high electrochemical capability.[21] However, no obvious oxygen reduction peak is observed in MSAC-600 due to its poor ORR activity. Among them, MSAC-750 presents the highest current density (0.26 mA cm^{-2}), higher than that of Pt/C (0.19 mA cm^{-2}), MSAC-700 (0.18 mA cm^{-2}), MSAC-800 (0.17 mA cm^{-2}) and MSAC-900 (0.12 mA cm^{-2}), indicating that MSAC-750 generates oxygen reduction reactions more easily under the same conditions. On the one hand, given that the internal reasonable porous structure of MSAC-750 provides enough reaction sites for ORR, MSAC-750 is provided with the highest current density. Furthermore, MSAC-750 has the highest content of pyridine-N and Fe-N_X, which allows for more active sites of the ORR.[8]

As shown in Fig. 6(a), the Tafel curve can also be used to study the catalytic performance of different MSAC catalysts. By virtue of the linear fitting ($R^2 \geq 0.99$) of the overpotential range of 80–120 mV in the Tafel curve, the exchange current density (i_0) of the catalyst can be obtained.[10] The exchange current density (i_0) is an important indicator reflecting the ORR charge

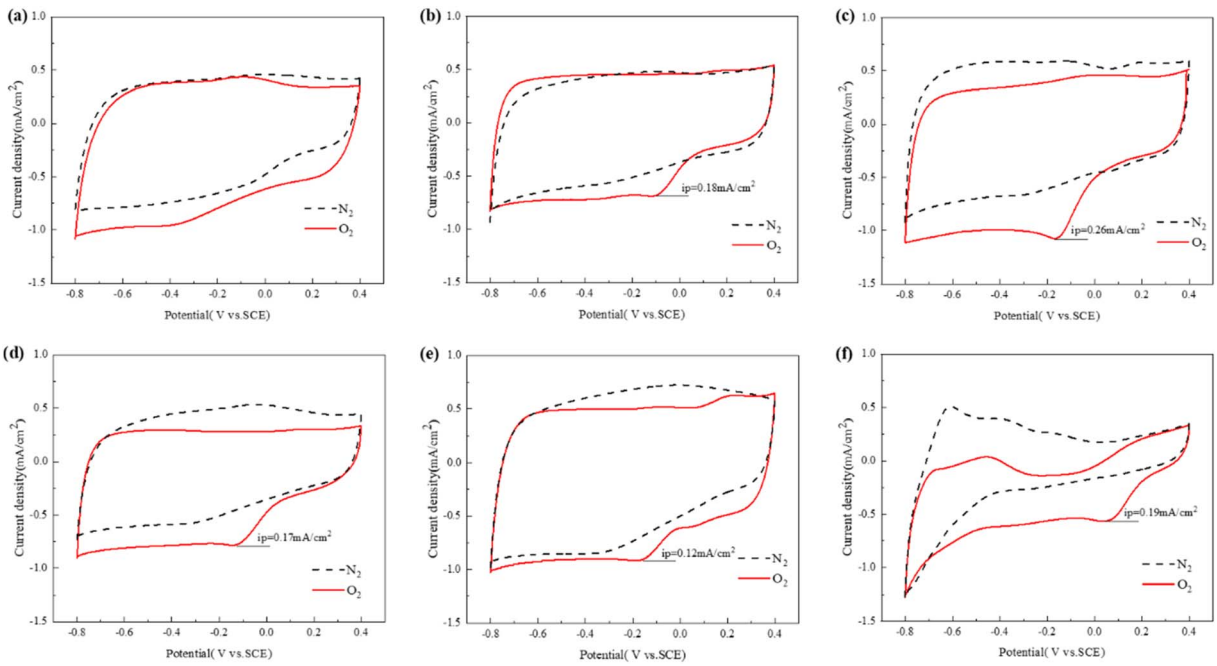

Fig. 5 CV results of the (a)–(e) MSAC-600, MSAC-700, MSAC-750, MSAC-800, MSAC-900, and (f) Pt/C in O_2 or N_2 saturated 50 mM PBS solution at a scan rate of 5 mV s^{-1}.

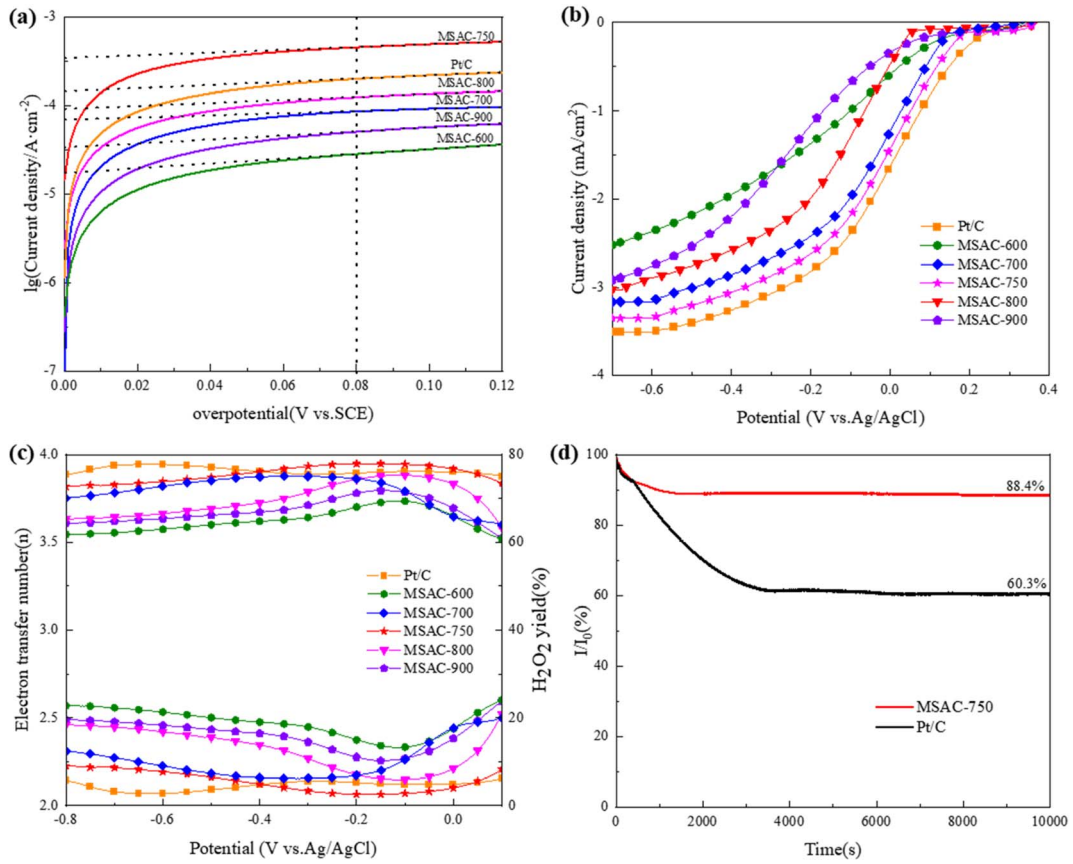

Fig. 6 (a) Tafel curves, (b) RRDE curves in O_2-saturated 50 mM PBS at a scan rate of 5 mV s^{-1} with 1600 rpm, (c) the electron transfer numbers (n) and H_2O_2 yield of MSAC catalysts and Pt/C, (d) I–t chronoamperometric responses of MSAC-750 and Pt/C in O_2-saturated 50 mM PBS at 1600 rpm for 10 000 s.

transfer rate.[35] The exchange current density (i_0) value of each MSAC is listed in Table 2. MSAC-750 has the highest exchange current density i_0 (1.904×10^{-4} A cm^{-2}), which is approximately 24.3%, 52.1%, 63.7%, 82.4%, and 90.9% higher than Pt/C, MSAC-800, MSAC-700, MSAC-900 and MSAC-600, respectively. MSAC-600 has a low exchange current density (i_0), which may be caused by the low graphitization degree of the material. However, MSAC-900 has a low ORR performance, for its internal graphitized structure collapses at high temperatures.

Fig. 6(b) shows the ORR activity of these MSAC catalysts on the rotating ring disk electrode (RRDE). Among them, the MSAC-700, MSAC-750, MSAC-800, and Pt/C catalysts afford limiting disk currents of −3.16, −3.34, −3.02, and −3.50 mA cm^{-2}, respectively, while MSAC-600 and MSAC-900 do not reach the limit current due to their excessively low ORR kinetics. Based on previous studies, the onset potential (E_{onset}) and half-wave potential ($E_{1/2}$) were hereby used to characterize the activity of the catalyst.[36] The former is defined as the potential corresponding to 5% of the limiting current density, while the latter is defined as the potential corresponding to 50% of the limiting current density.[37] The values of these two parameters are listed in Table 2. As shown in Table 2, the onset potential E_{onset} (0.172 V) and half wave potential $E_{1/2}$ (−0.028 V) of MSAC-750 are higher than those of MSAC-700 (0.145 V and −0.042 V) and MSAC-800 (0.044 V and −0.123 V) and are slightly lower than those of the Pt/C catalyst (0.221 V and −0.016 V). This indicates that MSAC-750 has a charge exchange frequency and electrochemical performance similar to those of the Pt/C

Table 2 Electrochemical properties of the cathode catalysts

Catalysts	$i_0 \times 10^{-4}$ (A cm^{-2})	E_{onset} (V *vs.* Ag/AgCl)	$E_{1/2}$ (V *vs.* Ag/AgCl)	n	H_2O_2 yield (%)
MSAC-600	0.173	—	—	3.62	18.82
MSAC-700	0.690	0.145	−0.042	3.80	10.08
MSAC-750	1.904	0.172	−0.028	3.89	5.38
MSAC-800	0.912	0.044	−0.123	3.75	12.64
MSAC-900	0.335	—	—	3.68	19.95
Pt/C	1.442	0.221	−0.016	3.91	4.51

catalyst. To this end, MSAC-750 is expected to be used as a substitute for Pt/C in future MFC cathodes. Next, Fig. 6(c) reveals the number of electron transfers (n) and H_2O_2 yields in the ORR process of the MSAC-T catalyst. The electron transfer number (n) and H_2O_2 yield in the potential window of −0.80 to 0.10 are averaged, and the calculated values are listed in Table 2.[10] The electron transfer number (n) of MSAC-600 and MSAC-900 is close to 3.6, and the ORR catalytic activity of $4e^-$ is low, which is consistent with the previous CV curve and Tafel curve analysis. The electron transfer number (n) in the ORR process of the MSAC-750 catalyst is 3.89, rather close to Pt/C (3.91) and closest to the $4e^-$ oxygen reduction pathway in the MSAC-T catalyst. The H_2O_2 yield of MSAC-750 is 5.38%, indicating the low-level $2e^-$ oxygen reduction activity of MSAC-750.

Stability is an important parameter of the catalyst in practical applications.[38] The long-term stabilities of MSAC-750 and Pt/C for ORR were hereby evaluated by chronoamperometry in O_2-saturated 50 mM PBS solution at a rotation rate of 1600 rpm, and the results are shown in Fig. 6(d). MSAC-750 is found to have a current retention of 88.4% after 10 000 s measurement, higher than 60.3% of Pt/C, illustrating the superior durability of the MSAC-750 material. The stability test [Fig. S5(a)†] based on the CV methods in 50 mM PBS solution after 1000 cycles indicates little difference with the initial CV and the ORR peak, and the current density of the MSAC-750 catalyst presents only a negative shift of 11 mV and 0.05 mA cm^{-2}, respectively. As shown in Fig. S5(b),† the output voltage of MSAC-750 cathode MFC is stabilized at about 0.42 V after continuous operation for 400 h, while that of Pt/C cathode MFC decreases from 0.4 V to 0.36 V, which is consistent with the previous analysis of chronoamperometry curves. These experiments reveal the excellent long-term durability of MSAC-750.

3.3 Microbial fuel cell experiments

To accurately evaluate the power generation capacity and pollutant removal capacity of each MSAC and Pt/C catalyst in practical applications, these catalysts were applied to the MFC cathode. The output voltage of each MSAC and Pt/C catalyst cathode MFC during stable operation is shown in Fig. 7(a). The maximum voltage of the MSAC-750 catalyst is 0.425 V, which is 1.24, 1.16, 1.11, 1.14 and 1.05 times that of the MSAC-600 (0.341 V), MSAC-700 (0.365 V), MSAC-800 (0.381 V), MSAC-900 (0.371 V) and Pt/C catalysts (0.402 V), respectively, indicating the strongest power generation capacity of the MSAC-750 catalyst. Additionally, the maximum output voltage of the commercial Pt/C catalyst cathode MFC drops to 0.385 V after 150 h of operation. The output voltage of the MFC with the MSAC-750 cathode shows almost no change and remains at a level of approximately 0.42 V. It is thus speculated that the following two reasons may reasonably explain the rapid decline of the output voltage in the Pt/C catalyst cathode MFC: First, on the

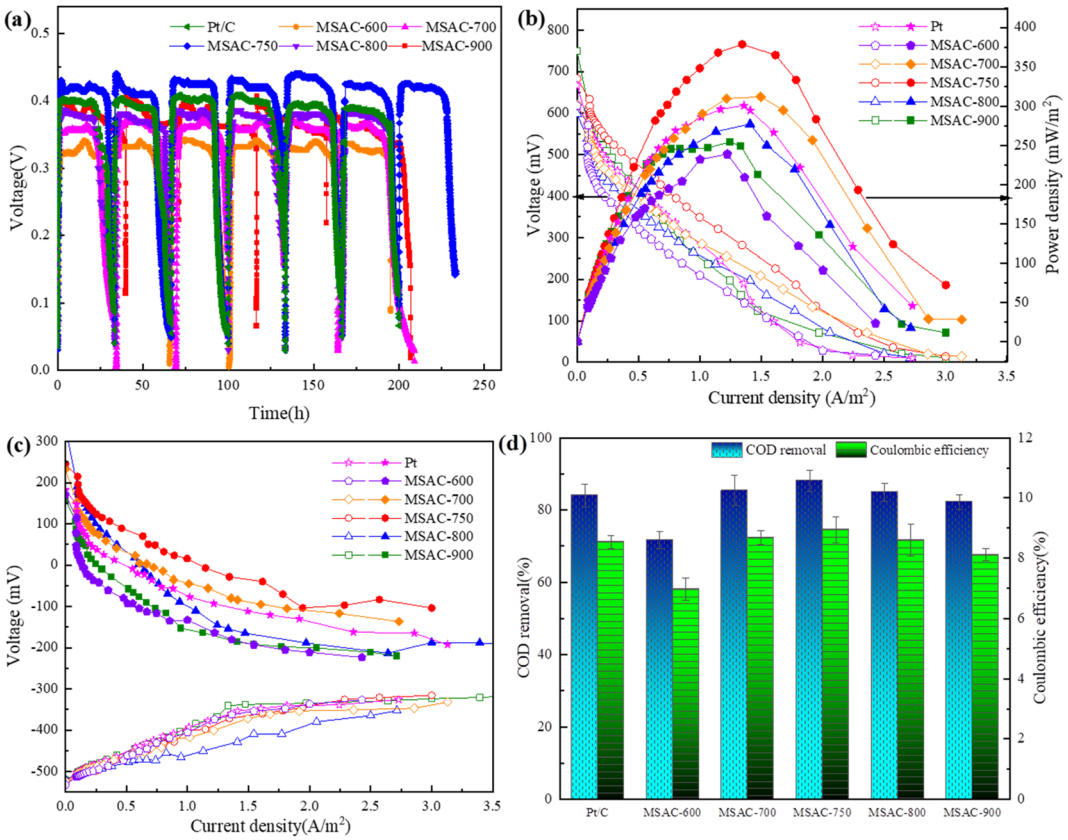

Fig. 7 (a) Voltage output for 250 h, (b) power density curves and polarization curves, (c) cathode and anode polarization curves, and (d) COD removal and CE of MFCs with the MSAC and Pt/C catalyst.

Table 3 Comparison of the performance of MFCs with that in previous studies

Anode material	Cathode catalyst	Output voltage (V)	Maximum power density (mW m^{-2})	Ref.
Carbon paper	Pt/C	0.38	261.0	42
Carbon cloth	Co–N–C-2	0.45	399.7	43
Carbon felt	EPGC-800-2	0.38	667.1	8
Carbon felt	WRC-700	0.27	262.2	7
Carbon felt	MPC-800	0.47	240.0	15
Carbon felt	MSAC-750	0.43	378.7	This study

one hand, the microbial pollution in the MFC may lead to the reduction of the catalytic activity of the Pt/C catalyst; on the other hand, the ions in the solution may lead to Pt poisoning or deactivation.[39] The above situation can be avoided by using the MSAC-T catalyst. The MSAC-T catalyst is doped with Fe and N elements so that it can produce charged defects and adjust the surface polarity of the carbon skeleton, making it not easily poisoned and inactivated. Second, the porous structure inside the MSAC-T catalyst prevents the active sites from being covered by microorganisms, thus facilitating the more effective transmission of oxygen molecules and improving the durability of their long-term operation.[16]

The power density curve and polarization curve are important parameters that reflect the discharge performance of an MFC. We select a stable operation cycle of the MFC, measure its power density and polarization curve by adjusting the external resistance, and record the electrode potential of the anode and cathode. The open-circuit voltage and power density of the MSAC-T and Pt/C catalysts are shown in Fig. 7(b). The maximum power density of the MFC with the MSAC-750 catalyst is 378.68 mW m^{-2}, which is 1.58, 1.21, 1.36, and 1.48 times that of MSAC-600 (238.36 mW m^{-2}), MSAC-700 (312.00 mW m^{-2}), MSAC-800 (277.20 mW m^{-2}), and MSAC-900 (254.25 mW m^{-2}), respectively, and is approximately 20% higher than that of 300.85 mW m^{-2} with the Pt/C catalyst. Besides, the open-circuit voltage of the MFC with different catalysts can be obtained from the polarization curve in Fig. 7(b). Compared with MSAC-600 (0.598 V), MSAC-700 (0.682 V), MSAC-800 (0.620 V) and MSAC-900 (0.618 V), MSAC-750 achieves the highest open-circuit voltage (0.749 V), which is consistent with the previous electrochemical test results. This is because the N and Fe elements of the MSAC-750 catalyst successfully infiltrate into the carbon skeleton and form graphite structures, such as FeC_3 and Fe-N_X configurations, thereby leading to a better electron transfer ability and more ORR active sites.[32] Then, the polarization curves of the anode and cathode were further measured. As shown in Fig. 7(c), the difference between the anode polarization curves is small, while the changing trend of the cathode polarization curve is similar to that of the power density curve, indicating that the difference in the power generation capacity between MFCs is mainly attributed to the cathode catalyst.[40]

The actual wastewater treatment capacity and electron generation efficiency of the MFC can be described by the COD removal rate and the coulombic efficiency, respectively. As shown in Fig. 7(d), the COD removal rate of most catalyst cathode MFCs is relatively high. Only the MSAC-600 cathode MFC has the lowest COD removal rate (71.57 ± 2.34%) due to its lack of pore structure and ORR active sites in the cathode catalyst. The MSAC-750 cathode MFC possesses the highest COD removal rate (88.10 ± 2.96%), followed by MSAC-700 (85.39 ± 4.22%), MSAC-800 (84.93 ± 2.51%), Pt/C (84.06 ± 3.14%) and MSAC-900 (82.22 ± 1.99%). Besides, the MSAC-750 cathode MFC has the highest CE (8.94 ± 0.52%), followed by MSAC-700 (8.68 ± 0.42%), MSAC-800 (8.59 ± 0.23%), Pt/C (8.53 ± 0.21%), MSAC-900 (8.11 ± 0.21%) and MSAC-600 (6.97 ± 0.36%). The MSAC-750 cathode MFC is provided with the highest COD removal rate and a high coulombic efficiency, which is mainly attributed to its high conductivity and good ORR catalytic activity. Previous characterization tests have confirmed the high graphitization structure and the highest exchange current density ($i_0 = 1.904 \times 10^{-4}$ A cm^{-2}) of the MSAC-750 material, which result in the fastest charge transfer rate and a lower ORR activation barrier, helpful for transferring more electrons to the anode surface. This efficient electronic recovery function considerably improves the COD removal rate and the coulombic efficiency of the MSAC-750 MFC catalyst.[41]

Eventually, the performance of the MSAC-750 cathode MFC was compared with that described in other studies. As shown in Table 3, the output voltage of the MSAC-750 cathode MFC is equivalent to or slightly better than that of some reported catalysts. However, considering the low content of electricity-producing bacteria in anaerobic activated sludge bacteria of the hereby adopted sewage treatment plant and the existence of some competitive bacteria, including methanogens, denitrifying bacteria, and desulfurizing bacteria, the maximum power density of the MSAC-750 cathode MFC is slightly lower than that of some cathode oxygen reduction catalysts. Another reason may be that the high internal resistance of the MFC device loaded with the MSAC-750 catalyst in this experiment affects the output power.

4. Conclusions

In summary, by activating the waste macadamia shell using K_2FeO_4 and urea, Fe/N codoped porous graphite biochar was hereby synthesized as an ORR catalyst for MFC cathodes under high-temperature pyrolysis. Among the tested temperatures, 750 °C is the best preparation temperature. The MSAC-750 catalyst prepared at this temperature has a high specific surface area (1670.3 m^2 g^{-1}), a graphitization structure, and

high pyridine-N and Fe-N_X contents. In terms of electrochemical activity, MSAC-750 presents an initial potential of 0.172 V and a half-wave potential of −0.028 V (compared with Ag/AgCl), and its ORR process is dominated by a 4-electron transfer pathway. In addition, the MSAC-750 catalyst was applied to an MFC, and it is found that in terms of the operating voltage, COD removal rate, and maximum power density, its performance is close to that of Pt/C, or is even better. More importantly, MSAC-750 shows more stable catalytic activity than Pt/C catalyst because of its carbon catalyst characteristics. In this case, not only a green synthesis method was hereby proposed for MFC high-efficiency cathode ORR catalysts, but also natural biomass waste was made full use of to achieve sustainable energy development.

Author contributions

Haoming Ning: conceptualization, writing – original draft, writing – review & editing. Zhi Zhang: funding acquisition, writing – review & editing, supervision. Chunhai Shi: visualization, supervision. Xiaolei Ma: investigation. Jian Li: writing – review & editing. Hongyi Zhu: writing – review & editing. Jiawei Hu: investigation.

Conflicts of interest

The authors declare that they have no known competing financial interests or personal relationships that could have appeared to influence the work reported in this paper.

Acknowledgements

This work is financially supported by the Ministry of Housing and Urban-Rural Development of China (grant numbers 2021-K-112). We also appreciate the Analysis and Testing Center of Chongqing University.

References

1 C. Santoro, C. Arbizzani, B. Erable and I. Ieropoulos, *J. Power Sources*, 2017, **356**, 225–244.
2 B. M. An, S. j. Seo, S. Hidayat and J. Y. Park, *J. Ind. Eng. Chem.*, 2020, **81**, 1–6.
3 K. Obileke, H. Onyeaka, E. L. Meyer and N. Nwokolo, *Electrochem. Commun.*, 2021, **125**, 107003.
4 K. Zhong, L. Huang, M. Li, Y. Dai, Y. Wang, J. Zuo, H. Zhang, B. Zhang, S. Yang, J. Tang, J. Yan and M. Su, *Int. J. Hydrogen Energy*, 2019, **44**, 30127–30140.
5 Y. Sun, Y. Duan, L. Hao, Z. Xing, Y. Dai, R. Li and J. Zou, *ACS Appl. Mater. Interfaces*, 2016, **8**, 25923–25932.
6 B. Zheng, J. Wang, Z. Pan, X. Wang, S. Liu, S. Ding and L. Lang, *J. Porous Mater.*, 2020, **27**, 637–646.
7 K. Zhong, M. Li, Y. Yang, H. Zhang, B. Zhang, J. Tang, J. Yan, M. Su and Z. Yang, *Appl. Energy*, 2019, **242**, 516–525.
8 Z. T. Zha, Z. Zhang, P. Xiang, H. Zhu, B. Zhou, Z. Sun and S. Zhou, *RSC Adv.*, 2021, **11**, 1077–1085.
9 X. Wang, X. Gong, L. Peng, Z. Yang and Y. Liu, *Bioelectrochemistry*, 2019, **127**, 104–112.
10 H. Zhu, Z. Zhang, Y. Zhou, X. Jiang, F. Cai, Y. Bai and H. Ning, *J. Water Process. Eng.*, 2022, **45**, 102471.
11 Z. W. Sun, C. Srinivasakannan, J. S. Liang and X. H. Duan, *Arabian J. Sci. Eng.*, 2019, **44**, 5443–5456.
12 L. Hou, Z. Hu, X. Wang, L. Qiang, Y. Zhou, L. Lv and S. Li, *J. Colloid Interface Sci.*, 2019, **540**, 88–96.
13 Q. Ren, S. Hu, L. He, F. Wu, Z. Wu, Z. Lei, S. Su, Y. Wang, L. Jiang and J. Xiang, *Waste Manage.*, 2021, **125**, 145–153.
14 K. Y. Chen, X. B. Huang, C. Y. Wan and H. Liu, *Chem. Commun.*, 2015, **51**, 7891–7894.
15 Z. T. Zha, Z. Zhang, P. Xiang, H. Y. Zhu, X. Shi and S. Chen, *Sci. Total Environ.*, 2021, **764**, 142918.
16 J. Li, X. Li, H. Chen, D. Xiao, J. Li and D. Xu, *J. Electroanal. Chem.*, 2020, **865**, 114133.
17 G. X. Lin, R. G. Ma, Y. Zhou, Q. Liu, C. Hu, M. H. Yang and J. C. Wang, *Appl. Mater. Today*, 2018, **13**, 174–181.
18 Z. T. Zha, Z. Zhang, P. Xiang, H. Zhu, X. Shi and S. Chen, *Sci. Total Environ.*, 2021, **764**, 142918.
19 Y. T. Tan, J. N. Ren, X. M. Li, L. J. He, C. M. Chen and H. B. Li, *New J. Chem.*, 2022, **46**, 14338–14345.
20 W. T. He, R. G. Ma, Y. F. Zhu, M. J. Yang and J. C. Wang, *J. Inorg. Mater.*, 2019, **34**, 1115–1122.
21 P. P. Chen, J. B. Zang, S. Y. Zhou, S. P. Jia, P. F. Tian, H. X. Cai, H. W. Gao and Y. H. Wang, *Carbon*, 2019, **146**, 70–77.
22 N. Hossain, S. Nizamuddin, P. Selvakannan, G. Griffin, S. Madapusi and K. Shah, *Chemosphere*, 2022, **291**, 132760.
23 I. Toda, H. Toda, H. Akasaka, S. Ohshio, S. Himeno and H. Saitoh, *J. Ceram. Soc. Jpn.*, 2013, **121**, 464–466.
24 D. Ma, Y. Yang, B. Liu, G. Xie, C. Chen, N. Ren and D. Xing, *Chem. Eng. J.*, 2021, **408**, 127992.
25 H. Yuan, Y. Hou, Z. Wen, X. Guo, J. Chen and Z. He, *ACS Appl. Mater. Interfaces*, 2015, **7**, 18672–18678.
26 G. Lin, R. Ma, Y. Zhou, Q. Liu, C. Hu, M. Yang and J. Wang, *Appl. Mater. Today*, 2018, **13**, 174–181.
27 X. Q. Hao, W. H. Chen, Z. Q. Jiang, X. N. Tian, X. G. Hao, T. Maiyalagan and Z. J. Jiang, *Electrochim. Acta*, 2020, 362.
28 X. K. Wang, Z. Zhang, H. Y. Gai, Z. K. Chen, Z. Y. Sun and M. H. Huang, *Mater. Today Energy*, 2020, 17.
29 Y. Sun, Y. Q. Duan, L. Hao, Z. P. Xing, Y. Dai, R. Li and J. L. Zou, *ACS Appl. Mater. Interfaces*, 2016, **8**, 25923–25932.
30 Z. Q. Xu, J. H. Ma, M. H. Shi, Y. H. Xie and C. Feng, *J. Colloid Interface Sci.*, 2018, **523**, 144–150.
31 Y. H. Su, H. L. Jiang, Y. H. Zhu, W. J. Zou, X. L. Yang, J. D. Chen and C. Z. Li, *J. Power Sources*, 2014, **265**, 246–253.
32 G. Y. Zhong, M. J. Xu, S. R. Xu, X. B. Fu, W. B. Liao and Y. J. Xu, *Int. J. Energ Res.*, 2021, **45**, 10393–10408.
33 M. Shi, J. Ma, Z. Yao, Z. Li, H. Mi and Y. Xie, *J. Electroanal. Chem.*, 2019, **839**, 141–148.
34 S. Pérez-Rodríguez, D. Sebastián, C. Alegre, T. Tsoncheva, N. Petrov, D. Paneva and M. J. Lázaro, *Electrochim. Acta*, 2021, **387**, 138490.
35 Y. Liu, Y. S. Fan and Z. M. Liu, *Chem. Eng. J.*, 2019, **361**, 416–427.

36 X. Wang, L. Zou, H. Fu, Y. Xiong, Z. Tao, J. Zheng and X. Li, *ACS Appl. Mater. Interfaces*, 2016, **8**, 8436–8444.
37 F. Y. Zheng, R. Li, S. Ge, W. R. Xu and Y. Zhang, *J. Power Sources*, 2020, **446**, 227356.
38 X. Fu, Y. Liu, X. Cao, J. Jin, Q. Liu and J. Zhang, *Appl. Catal., B*, 2013, **130–131**, 143–151.
39 F. Pan, Z. Cao, Q. Zhao, H. Liang and J. Zhang, *J. Power Sources*, 2014, **272**, 8–15.
40 J. Wang, P. Tian, K. Li, B. Ge, D. Liu, Y. Liu, T. Yang and R. Ren, *Bioresour. Technol.*, 2016, **222**, 107–113.
41 H. Y. He, M. Wang, Y. Zhang and J. S. Zhao, *J. Solid State Electrochem.*, 2017, **21**, 1639–1651.
42 J. Jang, S. H. Lee and K. J. Goo, *Microbiol. Biotechnol. Lett.*, 2010, **38**, 461–466.
43 J. C. Li, X. T. Wu, L. J. Chen, N. Li and Z. Q. Liu, *Energy*, 2018, **156**, 95–102.